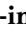# Heptanol-mediated phase separation determines phase preference of molecules in live cell membranes

Anjali Gupta[1] , Danqin Lu[1,2], Harikrushnan Balasubramanian[1] , Zhang Chi[3], and Thorsten Wohland[1,3]*

[1]Department of Biological Sciences and Centre for Bioimaging Sciences (CBIS), National University of Singapore (NUS), Singapore, Singapore; [2]School of Chemistry and Molecular Engineering, East China Normal University, Shanghai, China; and [3]Department of Chemistry, National University of Singapore (NUS), Singapore, Singapore

Abstract The localization of many membrane proteins within cholesterol- and sphingolipid-containing microdomains is essential for proper cell signaling and function. These membrane domains, however, are too small and dynamic to be recorded, even with modern super-resolution techniques. Therefore, the association of membrane proteins with these domains can only be detected with biochemical assays that destroy the integrity of cells require pooling of many cells and take a long time to perform. Here, we present a simple membrane fluidizer–induced clustering approach to identify the phase-preference of membrane-associated molecules in individual live cells within 10–15 min. Experiments in phase-separated bilayers and live cells on molecules with known phase preference show that heptanol hyperfluidizes the membrane and stabilizes phase separation. This results in a transition from nanosized to micronsized clusters of associated molecules allowing their identification using routine microscopy techniques. Membrane fluidizer-induced clustering is an inexpensive and easy to implement method that can be conducted at large-scale and allows easy identification of protein partitioning in live cell membranes.

Supplementary keywords fluidizers • phase separation • phases • membranes • heptanol • epidermal growth factor receptor • alcohols • assay • clustering • MFIC

Plasma membranes (PMs) are complex entities composed of a diversity of lipids and proteins that associate in different combinations, thereby resulting in PM heterogeneities. These heterogeneities exist in the form of protein clusters, lipid–lipid complexes, or combinations thereof, e.g., cholesterol sphingolipids or protein–lipid complexes (1, 2). In addition to the preferential interaction of these molecules with each other, there is a dynamic cytoskeleton network and extracellular matrix that influences the spatial organization of heterogeneities in the PMs (3, 4). PMs are extremely dynamic and are highly susceptible to change their physical properties and organization. Upon interaction with membrane-active compounds, such as peptides or anesthetics, membranes undergo a reversible modulation of spatial organization and membrane order (5–12). Membrane proteins often reside in a specific lipid environment in their resting state, and they change their environment upon activation (13). With increasing evidence, it is now realized that dynamic changes in the lipid environment of these proteins are essential for their functionality and regulation. The lipid environment of signaling proteins is hypothesized to influence the signal transduction originating at the PM (14–16). It was recently shown that specific structural characteristics of proteins such as palmitoylation, length of the transmembrane segment, and type of amino acids in the transmembrane region could determine their preference for a certain phase (17). However, the identity of the lipid environment surrounding the signaling proteins remains controversial, primarily because most of the existing literature relies on data obtained from indirect and artifact-prone methods (18, 19). The reason why indirect methods have been used to detect membrane domains is that the size of domains is typically below the diffraction limit, and thus, they are inaccessible by routine imaging methods. Moreover, due to their dynamic nature, membrane domains typically last from microseconds to seconds and are often difficult to detect.

To examine the complex PM structure and dynamics, artificially reconstituted model membranes have contributed significantly (20–29). However, they cannot recapitulate every physiologically relevant attribute. For instance, although model membranes can be tuned to exhibit micron-sized domains of a specific phase (liquid disordered and liquid-ordered), it is nearly impossible to visualize domains directly in cell membranes as the domains in PMs are much smaller and are very sensitive, e.g., even giant plasma membrane

vesicles do not keep the same organization as a live cell PM ([1], [17], [30]). Therefore, there is a clear need of simple methods that can detect the phase preference of membrane proteins in live intact cell membranes. Biochemical methods that have been used to differentiate the proteins that localize in the raft and nonraft phases include detergent-resistant extraction ([31]), immunostaining ([32]), and cell fractionation followed by mass spectrometry ([33]). However, these methods are artifact-prone as either they involve the use of nonphysiological experimental conditions or require fixed samples. Due to these reasons, fluorescence-based methods combined with live-cell imaging and spectroscopy (e.g., FCS diffusion law) are alternatives for determining the membrane heterogeneities ([34]–[38]). In previous studies, phase-specific fluorescent dyes and protein anchors have been used to understand the dynamic properties of the individual phases in live cell membranes ([36], [39]). Despite the wide usage of such methods, they have been difficult to implement due to the requirement of specialized instrumentation, and they also have some exceptions that pose problems in their interpretation ([40]–[42]).

In this work, we present a novel membrane fluidizer–induced clustering (MFIC) methodology to determine the localization of molecules in live cell membranes. In this study, we use heptanol as a membrane-fluidizing agent and show using total internal reflection fluorescence microscopy (TIRFM) that there is reversible reorganization in the cell membrane as a result of heptanol treatment. The molecules that reside in cholesterol-dependent domains segregate into micron-sized clusters, while molecules that reside outside the cholesterol-dependent domains stay dispersed. We test this assay in both model membranes and live intact cell membranes using several molecules with known phase preference. Moreover, we use this method to probe the localization of signaling-related proteins such as epidermal growth receptor factor (EGFR), IL-2Rα, K-Ras, and H-Ras. Furthermore, we test this method on other cell lines to ensure the universality of this method across different cell membranes. This method is an inexpensive, fast (~min), and minimally invasive way to determine whether a molecule resides within lipid domains in live cells.

MATERIALS AND METHODS

Reagents

The lipids 1,2-dioleoyl-sn-glycero-3-phosphocholine (DOPC), 1,2-dipalmitoyl-sn-glycero-3-phosphocholine (DPPC), and cholesterol (Chol) were used in this work. Head group–labeled rhodamine dye 1,2-dimyristoyl-sn-glycero-3-phosphoethanolamine-N-(lissamine rhodamine B sulfonyl) (ammonium salt) (14:0 Liss Rhod PE) was used as the fluorophore to label supported lipid bilayers. The lipids and dye were purchased from Avanti Polar Lipids (Alabama) and dissolved in chloroform.

1,1′-dioctadecyl-3,3,3′,3′-tetramethylindocarbocyanine perchlorate (DiI-C_{18}, #D3911), octadecyl rhodamine B chloride (#O246), and CTxB-555 (cholera toxin subunit B [recombinant] with Alexa Fluor 555 conjugate, #C34776) were purchased from Invitrogen (Thermo Fisher Scientific, Singapore). They were dissolved in anhydrous dimethyl sulfoxide (#276855, Sigma-Aldrich, Singapore) to prepare the stock solutions. The fluidizer 1-heptanol 98% (#H2805) was purchased from Sigma-Aldrich (Singapore).

An Alexa Fluor 488–conjugated EGFR monoclonal antibody was purchased from Cell Signaling Technology (EGF Receptor [D38B1] XP Rabbit mAb [Alexa Fluor 488 Conjugate], #5616S, MA).

Supported lipid bilayer preparation

All glassware (slides, coplin jars, and round-bottom flasks) were cleaned thoroughly with an alkaline cleaning solution (Hellmanex III, Hellma Analytics, Müllheim, Germany) using sonication (Elmasonic S30H, Elma Schmidbauer GmbH, Singen, Germany) for 30 min. They were then washed with ultrapure water (Milli-Q, Merck, NJ), submerged in 2 M sulfuric acid, and sonicated again for 30 min. After washing the glassware with deionized water and immersing them in the water, a final sonication was done for another 30 min.

A silicone elastomer (SYLGARD 184 Silicone Elastomer Kit, Dow, MI) was filled in an O-ring mold and cured at 65°C overnight. The O-rings (1.5 cm inner diameter) were carefully removed using forceps and attached to a slide using the silicone elastomer, followed by curing at 65°C for 3 h.

DOPC:DPPC:Chol (4:3:3) solution (500 μM) and 100 nM 1,2-dimyristoyl-sn-glycero-3-phosphoethanolamine-N-(lissamine rhodamine B sulfonyl) were mixed thoroughly in a round-bottom flask and evaporated in a rotary evaporator (Rotavapor R-210, Büchi, Flawil, Switzerland) for 3–4 h until a thin lipid film was formed. The lipid film was dissolved in 2 ml of a buffer solution (10 mM Hepes, 150 mM NaCl, pH 7.4) and sonicated until the solution became clear, indicating the formation of large unilamellar vesicles. Lipid solution (200 μl) was added into an O-ring attached to a slide and incubated at 65°C for 1 h to allow vesicle fusion and formation of the supported lipid bilayer (SLB). The SLB was cooled to room temperature (25°C) for 30 min and then washed with the buffer solution multiple times to eliminate the unfused vesicles. SLB measurements were done at 37°C.

Plasmids

The green fluorescent protein–tagged glycosylphosphatidylinositol-anchored protein (GPI-GFP plasmid) was a kind gift of John Dangerfield (Anovasia Pte Ltd., Singapore). The plasmids IL2Rα-EGFP (Addgene plasmid #86055), mEGFP-HRas (Addgene plasmid #18662), and pLVET-HA-K-RasG12V-IRES-GFP (Addgene plasmid #107140) were purchased from Addgene (MA). The construction of EGFR-mApple has been previously described ([43]). The EGFR-mEGFP plasmid was constructed in the same way as EGFR-mApple. Lifeact-mRFPruby (Addgene plasmid #51009; a gift originally from Rusty Lansford) was gifted by Wu Min (CBIS, NUS) ([44]).

The sequences of the transmembrane domain of linker for activation of T-cells (WT-trLAT) and a mutant with all the transmembrane domain (TMD) amino acids (except the palmitoylation sites) mutated to leucines (allL-trLAT) have been previously described ([45]). DNA duplexes were designed with the trLAT sequences flanked by AgeI and SpeI restriction

sites on the 5′ and 3′ ends, respectively, with a 6-base linker between them. The duplex DNA sequences were synthesized and purchased from Integrated DNA Technologies Pte. Ltd. (Singapore). The EGFR-mApple and EGFR-mEGFP plasmids were digested with AgeI (AgeI-HF, R3552S, New England BioLabs, MA) and SpeI (SpeI-HF, R3133S, New England Bio-Labs) to create the plasmid backbones. The WT-trlAT and allL-trlAT sequences were also digested with AgeI and SpeI to create the inserts. The backbones and inserts were ligated using T4 DNA ligase (M0202S; New England BioLabs) to create four plasmids—WT-trlAT-mEGFP, WT-trlAT-mApple, allL-trlAT-mEGFP, and allL-trlAT-mApple.

Cell culture

The protocol detailing the steps in the preparation of live cell samples for fluorescence applications is provided in Protocol Exchange (46). SH-SY5Y (#CRL-2266) and HeLa (#CCL-2) cells were obtained from ATCC (Manassas, VA). They were cultivated in Dulbecco's Modified Eagle Medium (DMEM/High glucose with L-glutamine, without sodium pyruvate—#SH30022.FS) (HyClone, GE Healthcare Life Sciences, UT) supplemented with 10% fetal bovine serum (FBS; #10270106, Gibco, Thermo Fisher Scientific, Singapore) and 1% penicillin-streptomycin (#15070063, Gibco, Thermo Fisher Scientific), at 37°C in a 5% (v/v) CO_2 humidified environment (Forma Steri-Cycle CO_2 incubator, Thermo Fisher Scientific).

Cell cultures that were ~90% confluent were passaged. The spent media were removed from the culture flask and 5 ml 1× PBS (phosphate-buffered saline; without Ca^{2+} and Mg^{2+}) was used to wash the cells twice. TrypLE Express Enzyme (2 ml) (1×; #12604021, Gibco, Thermo Fisher Scientific, Singapore) was added, and the flask was placed in the CO_2 incubator for 2–3 min. Upon detachment of the cells, 5 ml culture media were added to the flask to inhibit trypsin. The cell suspension was centrifuged (#5810, Eppendorf, Hamburg, Germany) at 200 g for 3 min. The supernatant was discarded, and the cell pellet was resuspended in 5 ml 1× PBS. An automated cell counter (TC20, Bio-Rad, Singapore) was used to count the cells, and the required number of cells was used for the next step of cell membrane staining or transfection.

Cell membrane staining

After passaging, the required number of cells were seeded onto culture dishes (#P35G-1.5-20-C, MatTek, MA) containing culture media and allowed to attach for 24 h. DiI-C$_{18}$, R18, and CTxB-555 stock solutions were diluted to 100 nM working concentration in imaging medium (DMEM with no phenol red, #21063029, Gibco, Thermo Fisher Scientific) supplemented with 10% FBS. They were used for cell membrane staining. The media were removed and replaced with the working dye solution. The cells were placed in the CO_2 incubator for 20 min. Then, the dye solution was removed, and the cells were washed with 1× HBSS (Hank's Balanced Salt Solution, with Ca^{2+} and Mg^{2+}; #14025134; Gibco, Thermo Fisher) twice. DMEM without phenol red (#21063029; Gibco, Thermo Fisher Scientific, MA), hereafter called imaging media, was supplemented with 10% FBS and added to the cells before measurements.

Transfection

After passaging, the required number of cells was centrifuged at 200 g for 3 min. The supernatant was discarded, and the cells were resuspended in R buffer (Neon Transfection Kit, Thermo Fisher Scientific). Suitable amounts of plasmids were mixed with the cells for transfection. The cells were electroporated according to the manufacturer's protocol (electroporation settings: SH-SY5Y – pulse voltage = 1,200 V, pulse width = 20 ms, pulses = 3; HeLa – pulse voltage = 1,005 V, pulse width = 35 ms, pulses = 2) using Neon Transfection system (Thermo Fisher Scientific). After transfection, the cells were seeded onto culture dishes containing DMEM (with 10% FBS; no antibiotics). The cells were incubated in the CO_2 incubator for 20–48 h before the measurements.

Cell measurements

The transfected cells were washed twice with HBSS, and imaging media (with 10% FBS) were added before measurements. EGFR-transfected cells were starved for a few hours in imaging media (without FBS to prevent aberrant activation of EGFR) before measurements. Stock heptanol solution was filtered with a 0.2 μm syringe filter and added to the imaging media to obtain the working concentration of 5 mM. Measurements were done after 10–20 min of incubation.

For the two-color EGFR antibody measurements, the antibody was diluted 1:200 in imaging media and added to EGFR-transfected cells. The cells were incubated for 3 h in the CO_2 incubator. Subsequently, they were washed with HBSS twice, and imaging media were added. After initial imaging of the antibody labeling, 5 mM heptanol was added to the cells, and they were imaged.

Cell viability determined through trypan blue staining

To determine fraction of live cells in the sample before and after heptanol treatment, the samples were trypsinized, and trypan blue stain was mixed with the cells (Bio-Rad). The cells were counted using an automated cell counter (TC20, Bio-Rad) which provided the live cell fraction values.

Western blotting analysis of EGFR phosphorylation

Four 10 cm cell culture dishes (#353003, Corning, NY) were each seeded with 2×10^5 CHO-K1 cells transfected with 10 μg of EGFR-mApple. A mock transfection without any plasmid was also done. The transfected cells were incubated at 37°C with 5% CO_2 for 36 h. The cells were then washed with 1× HBSS and serum-starved in imaging DMEM for 4 h. Following this, three of the transfected samples were treated with 5 mM heptanol for 15 min, 100 ng/ml EGF for 20 min, and 5 mM heptanol for 15 min followed by 100 ng/ml EGF for 20 min, respectively.

A Western blot kit (#12957, Western Blotting Application Solutions Kit, Cell Signaling Technology) was used for performing the Western blots as per the manufacturer's protocol. All the cells were lysed using the provided cell lysis buffer, and the cell extracts were sonicated using an ultrasonicator (VC 505, Sonics, CT). Sodium dodecyl sulphate–polyacrylamide gel electrophoresis was used to separate the proteins in the samples. Two 4%–20% precast polyacrylamide gels (#4561093, Mini-PROTEAN TGX Precast Protein Gels (10-well, 30 μl), Bio-Rad, CA) were processed in parallel—one gel was for probing with total EGFR primary antibody and the other gel with phosphorylated EGFR primary antibody. A 10–250 kDa protein ladder (#1610373, Precision Plus Protein All Blue Prestained Protein Standards, Bio-Rad, CA) was also loaded along with the samples.

The protein bands were wet-transferred from each PAGE gel to a PVDF membrane (0.45 μm pore size). In each sample set of two membranes, one membrane was incubated in a primary antibody solution containing total EGFR polyclonal

antibody (#2232S, Cell Signaling Technology) and β-actin polyclonal antibody (#4967S, Cell Signaling Technology). The other membrane was incubated in a primary antibody solution containing phospho-EGFR (Y1173) monoclonal antibody (#4407S, Cell Signaling Technology) and β-actin polyclonal antibody. This was followed by washing, blocking, and incubation in the secondary antibody (#7074S, Cell Signaling Technology). An enhanced chemiluminescent substrate solution (#6883, SignalFire ECL Reagent, Cell Signaling Technology) was used, and the chemiluminescence was detected using an imager (ImageQuant LAS 4000, GE Healthcare Bio-Sciences AB, Uppsala, Sweden) equipped with a CCD camera. The CCD camera was operated after cooling to −25°C, and the images were saved as 16 bit tiff files.

Calculation of EGFR phosphorylation levels

The intensity counts were of the bands were first corrected for the background (area on membrane with no bands).

$$\langle I_{band,corrected}\rangle = \langle I_{band}\rangle - \langle I_{background}\rangle \qquad (1)$$

where $\langle I_{band,corrected}\rangle$ is the average corrected intensity of the band, $\langle I_{band}\rangle$ is the average original intensity of the band, and $\langle I_{background}\rangle$ is the average intensity of the background (area on membrane with no bands).

The β-actin (to normalize cell numbers) bands for corresponding lanes in the total EGFR and phosphorylated EGFR blots were normalized.

$$\langle I_{band,corrected}\rangle_{\beta,pE(nor)} = \frac{\langle I_{band,corrected}\rangle_{\beta,pE}}{\langle I_{band,corrected}\rangle_{\beta,tE}} \qquad (2)$$

where $\langle I_{band,corrected}\rangle_{\beta,pE(nor)}$ is the normalized average intensity of β-actin band in phosphorylated EGFR blot, $\langle I_{band,corrected}\rangle_{\beta,pE}$ is the original average intensity of β-actin band in phosphorylated EGFR blot, and $\langle I_{band,corrected}\rangle_{\beta,tE}$ is the original average intensity of β-actin band in total EGFR blot.

The EGFR bands for corresponding lanes in the total EGFR and phosphorylated EGFR blots were normalized to their respective normalized β-actin bands.

$$\langle I_{band,corrected}\rangle_{E,tE(nor)} = \frac{\langle I_{band,corrected}\rangle_{E,tE}}{\langle I_{band,corrected}\rangle_{\beta,tE}} \qquad (3)$$

$$\langle I_{band,corrected}\rangle_{E,pE(nor)} = \frac{\langle I_{band,corrected}\rangle_{E,pE}}{\langle I_{band,corrected}\rangle_{\beta,pE(nor)}} \qquad (4)$$

where $\langle I_{band,corrected}\rangle_{E,tE(nor)}$ is the normalized average intensity of EGFR band in total EGFR blot, $\langle I_{band,corrected}\rangle_{E,tE}$ is the original average intensity of EGFR band in total EGFR blot, $\langle I_{band,corrected}\rangle_{E,pE(nor)}$ is the normalized average intensity of EGFR band in phosphorylated EGFR blot, and $\langle I_{band,corrected}\rangle_{E,pE}$ is the original average intensity of EGFR band in phosphorylated EGFR blot.

The phosphorylation level was quantified as the ratio of the average intensity of the phosphorylated EGFR band and corresponding total EGFR band.

$$Phosphorylation = \frac{\langle I_{band,corrected}\rangle_{E,pE(nor)}}{\langle I_{band,corrected}\rangle_{E,tE(nor)}} \qquad (5)$$

Instrumentation

TIRF microscopy. An inverted epi-fluorescence microscope (IX83, Olympus, Singapore) with a motorized TIRF illumination combiner (cellTIRF-4Line IX3-MITICO, Olympus) and an oil-immersion objective (100×, NA 1.49, Apo N, Olympus) was used for the imaging measurements. 488 nm (LAS/488/100, Olympus) and 561 nm (LAS/561/100, Olympus) lasers were connected to the TIRF illumination combiner. The laser power (as measured at the back aperture of the objective) used for both the 488 nm laser and the 561 nm laser was ∼0.3 mW for the single-channel imaging and ∼0.1 mW for two-color imaging. The fluorescence emission was passed through a dichroic (ZT 405/488/561/640rpc, Chroma Technology Corp., VT) and emission filter (ZET405/488/561/640m, Chroma Technology Corp.) to an electron multiplying charge-coupled device (EMCCD; iXon^{EM}+ 860, 24 μm pixel size, 128 × 128 pixels, Andor, Oxford Instruments, UK) camera. For the dual-color measurements, a dual-emission image splitter (OptoSplit II, Cairn Research, Faversham, UK) equipped with an emission dichroic (FF560-FDi01, Semrock, NY) and band-pass emission filters (FF03-525/50-25 and BLP01-568R-25, Semrock) was used.

The using imaging total internal reflection fluorescence correlation spectroscopy (ITIR-FCS) measurements were carried out using another TIRF microscope (IX-71, Olympus) equipped with an oil-immersion objective (PlanApo, 100×, NA 1.45, Olympus) and an EMCCD (iXon 860, 24 μm pixel size, 128 × 128 pixels, Andor) camera. 488 nm (Spectra-Physics Lasers, CA) and 532 nm (Cobolt Samba, Sweden) lasers were used as the excitation sources that focused on the samples by a combination of two tilting mirrors and a dichroic mirror—495LP (Omega Optical, VT) for 488 nm and Z488/532M (Semrock) for 561 nm excitation, respectively. ∼0.3 mW laser power (as measured at the back focal plane of the objective) was used for both lasers.

For the cell measurements, 37°C temperature and 5% CO$_2$ atmosphere were maintained using an on-stage incubator (Chamlide TC, Live Cell Instrument, South Korea). Andor Solis (version 4.31.30037.0–64 bit) was used for image acquisition. The following camera settings were used: mode of image acquisition = kinetic, baseline clamp = "on" to minimize the baseline fluctuation, pixel readout speed = 10 MHz, maximum analog-to-digital gain = 4.7, vertical shift speed = 0.45 μs, EM gain = 300. A region of interest of size 5.04 × 5.04 μm^2 containing 21 × 21 pixels was selected on a cell. For FCS measurements, a stack of 50,000 frames was collected by the EMCCD with 1 ms recording time for DiI-C$_{18}$ and 2 ms for the other samples. For the measurements, a stack of 10 frames was collected at 20 ms exposure time, except for the two-color EGFR-antibody measurements where 100 ms was used.

Confocal microscopy. For large field of view imaging, a confocal laser scanning microscope (Fluoview FV1200-IX83, Olympus, Singapore) was used. A 10× (NA 0.4, UPLSAPO10X2, Olympus) and water-immersion 60× (NA 1.2, UPLSAPO60XW, Olympus) objectives were used for the imaging. An excitation dichroic mirror (DM405/488/543/635, Chroma Technology, VT) was used to reflect a 488 nm laser to the sample. The samples were illuminated with 10 μW laser power (as measured at the back focal plane of the objective). The fluorescence emission passed through a 120 μm (1 airy unit) confocal pinhole, the excitation dichroic mirror, and directed by an emission dichroic (560DCXR, Chroma Technology) through an emission filter (BA505-525, Olympus) to a GaAsP photomultiplier tube for detection. Images of 1,024 × 1,024

pixels (1,272 μm × 1,272 μm for 10× objective; 212 μm × 212 μm for 60× objective) were acquired using 40 μs pixel dwell time.

Data analysis

Estimation of diffusion coefficient from ITIR-FCS. After obtaining the image stacks, data analysis was performed using a home-written GPU-accelerated Imaging FCS 1.52 plugin in Fiji (43, 47) (https://github.com/ImagingFCS/Imaging_FCS_1_52). Fiji is an open-source image processing software, a distribution of ImageJ2 with bundled plugins for various image analysis. A step-by-step protocol detailing FCS data analysis is provided in Protocol Exchange (47). The fluorescence fluctuations at all pixels were calculated with the autocorrelation functions and fitted with the following equation after an exponential of polynomial bleach correction. Finally, quantitative maps of diffusion coefficient (D) were obtained as well as the FCS diffusion law intercept (τ_0) performed by the FCS diffusion law analysis of the same image stack.

$$G(\tau) = \frac{1}{N} \left[\frac{(p(\tau)) + \frac{\left(e^{-(p(\tau))^2} - 1\right)}{p(\tau)\sqrt{\pi}}}{(p(0)) + \frac{\left(e^{-(p(0))^2} - 1\right)}{p(0)\sqrt{\pi}}} \right]^2 + G_\infty; \quad p(\tau) = \frac{a}{\sqrt{4D\tau + \omega_0^2}}$$

(6)

Here $G(\tau)$ is the theoretical model of the autocorrelation function in dependence of the correlation time (τ). a is the pixel side length, ω_0 is the $1/e^2$ radius of the Gaussian approximation of microscope point spread function, while N is the number of particles. N, D, and G_∞ were all fitting parameters.

Cluster area fraction calculation. For calculation of the fractional cell area occupied by protein clusters (supplemental Fig. S1), intensity thresholding was applied using Fiji. The first thresholding step was to demarcate the cell from the background using a simple intensity threshold (Image → Adjust → Threshold). The second step was to threshold the clusters using the Renyi entropy algorithm (48) (Image → Adjust → Auto Threshold → RenyiEntropy). The algorithm had trouble choosing a threshold to identify clusters when the intensity differences between cluster and noncluster areas were small. To mitigate this, cells with high intensity differences between the cluster and noncluster areas were processed as 16 bit images, while cells with small intensity differences were converted and processed as 8 bit images.

The cells in resting state showed negligible clustering, and the algorithm failed to pick up any clusters. Therefore, for these cells, the thresholding was done manually to select the few clusters that were present.

The fractional area occupied by the clusters on the cell was calculated as:

$$Cluster\ area\ fraction = \frac{Number\ of\ pixels\ occupied\ by\ clusters}{Number\ of\ pixels\ occupied\ by\ cell}$$

Cluster size calculation. For calculation of the average cluster size (supplemental Fig. S1), all the images were converted to 8 bit, and intensity thresholding was done using the Renyi entropy algorithm (except for resting cells which were manually thresholded) as explained in the previous section. While the 8 bit conversion eliminated tiny dim clusters and biased toward choosing the larger and brighter clusters, it allowed better separation of closely spaced clusters resulting in more accurate average cluster size estimation. After thresholding, the clusters were analyzed in Fiji (Analyze → Analyze Particles) to determine the average cluster size. The results from Fiji had units of squared pixel which was reported in supplemental Fig. S1 after conversion to nm by calculating the square root and multiplying by pixel size (240 nm).

Statistical analyses. For the results in supplemental Fig. S1, a two-tailed homoscedastic *t*-test with 95% confidence interval was performed in Microsoft Excel. One-way ANOVA analysis was performed using an online calculator (https://www.statskingdom.com/180Anova1way.html). Tukey HSD posthoc test was also performed with 95% confidence interval to identify the difference levels between group pairs in ANOVA.

RESULTS

Heptanol induces hyperfluidization and domain segregation in model and live cell membranes
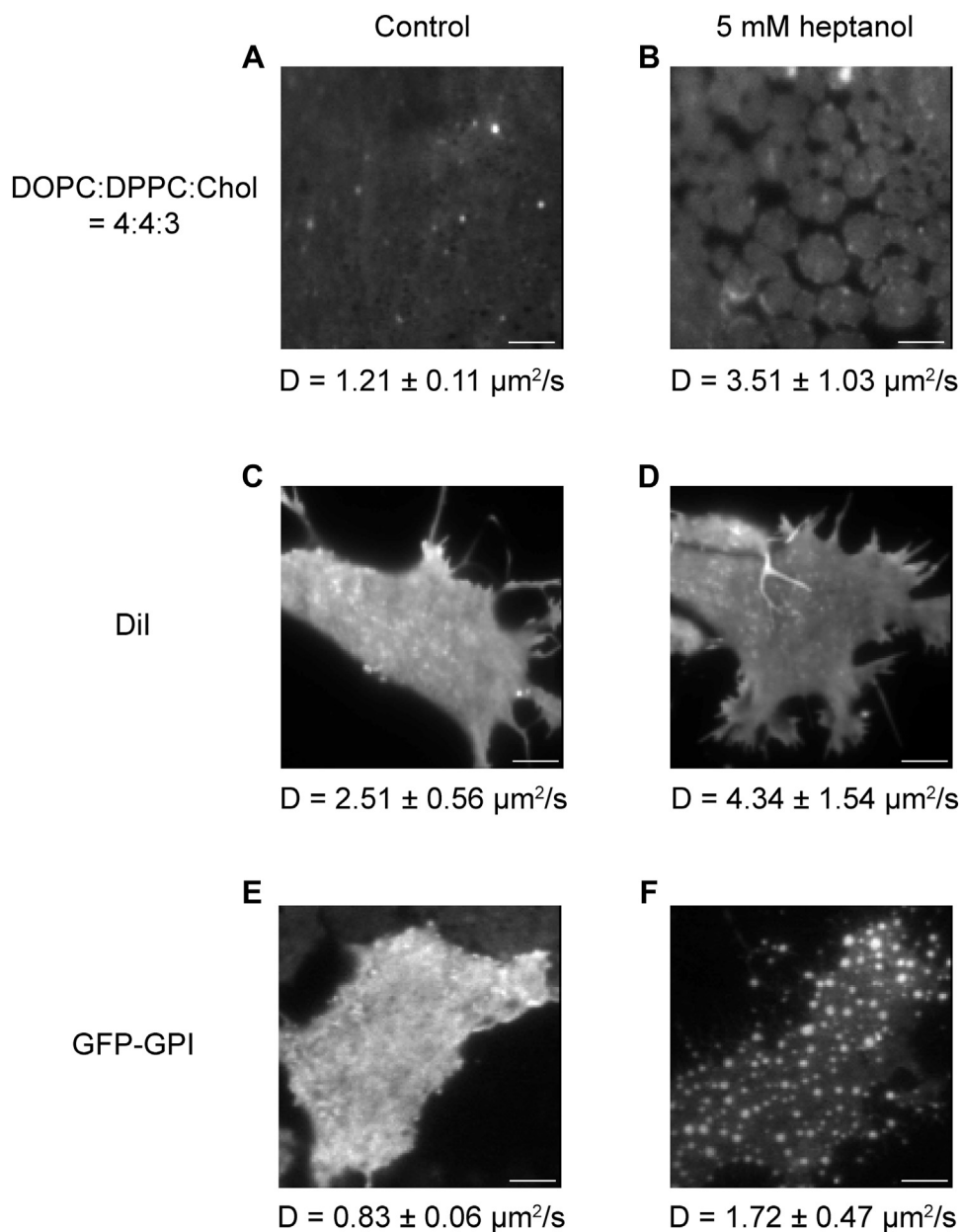
Fluidizers are membrane active compounds that increase the membrane order and alter the organization of membrane components. It has been reported that heptanol and related n-alkanols displace cholesterol from interactions with phospholipids thereby altering membrane structure (49). For alcohols with a carbon chain ≤7, an increase in carbon chain length results in higher membrane perturbing potency. However, as chain length exceeds 8, alcohols show reduced membrane perturbing potency (11). Previous work demonstrated that benzyl alcohol, a routinely used anesthetic, hyperfluidizes the membrane and induces the reorganization of domains (50, 51). Recently, it was shown that propofol also reorganizes cholesterol-dependent domains in cell membranes (52).

Inspired by these studies, we investigated the effect of heptanol, an alcohol-based anesthetic, on membrane dynamics and organization. To systematically evaluate the impact of heptanol on the organization and fluidity of membranes, we tested its effect on a ternary lipid bilayer exhibiting phase properties closer to cell membranes and subsequently on intact cell membranes. We measure the fluidity of the membrane using imaging ITIR-FCS, an imaging FCS modality that allows measurement of spatially resolved molecular diffusion over a whole region of interest in a single measurement.

DOPC:DPPC:Chol (4:4:3) lipid bilayers exhibit coexisting liquid-ordered (L_o) and liquid-disordered (L_d) (53) phases, mimicking the phase behavior of an intact cell membrane. As observed in a resting cell membrane, the size of domains in this bilayer is below the diffraction limit, thus it is optically homogeneous (**Fig. 1**A). To test the effect of heptanol on this bilayer, we treated the

bilayer with 5 mM heptanol and performed ITIR-FCS measurements on them immediately after the treatment. Our results show that upon heptanol treatment, the D of Rho-PE increases from 1.21 ± 0.11 $\mu m^2/s$ to 3.51 ± 1.03 $\mu m^2/s$ (Fig. 1A, B). Thus, as expected, heptanol fluidizes the membrane as inferred by an almost three times increase in D. Interestingly, we observed phase separation in the bilayer as there was formation of micron-sized lipid clusters 10 min after heptanol addition (Fig. 1A, B).

Intrigued by this observation, we extended these experiments to live cell membranes. We tested the heptanol-induced organizational changes on molecular probes (DiI-C_{18} and GFP-GPI) with known phase preferences in cell membranes. Here, we treat the cells with 5 mM heptanol and perform TIRF imaging and ITIR-FCS measurements. DiI-C_{18} localizes mainly in the fluid fraction of the membrane and has been used as a free diffusion marker, while GFP-GPI localizes in the cholesterol-dependent domains (13, 27, 36). Heptanol-

	Control	5 mM heptanol
DOPC:DPPC:Chol = 4:4:3	**A** $D = 1.21 \pm 0.11$ $\mu m^2/s$	**B** $D = 3.51 \pm 1.03$ $\mu m^2/s$
DiI	**C** $D = 2.51 \pm 0.56$ $\mu m^2/s$	**D** $D = 4.34 \pm 1.54$ $\mu m^2/s$
GFP-GPI	**E** $D = 0.83 \pm 0.06$ $\mu m^2/s$	**F** $D = 1.72 \pm 0.47$ $\mu m^2/s$

Fig. 1. Heptanol induces hyperfluidization and domain segregation in model and live cell membranes. Samples were treated with 5 mM heptanol. Representative TIRF images and the corresponding average diffusion coefficients (D) of different samples are shown here. A, B: Rhodamine-PE–labeled DOPC:DPPC:Chol (4:4:3) supported lipid bilayer before and after heptanol treatment. The D increases from 1.21 ± 0.11 $\mu m^2/s$ to 3.51 ± 1.03 $\mu m^2/s$ following heptanol treatment. C, D: DiI-C_{18}–labeled SH-SY5Y cells before and after the heptanol treatment. The D increases from 2.51 ± 0.56 $\mu m^2/s$ to 4.34 ± 1.54 $\mu m^2/s$ following heptanol treatment. E, F: GFP-GPI expressing SH-SY5Y cells before and after the heptanol treatment. The D increases from 0.83 ± 0.06 $\mu m^2/s$ to 1.72 ± 0.47 $\mu m^2/s$ following heptanol treatment. Experiments were repeated at least four times. The scale bars represent 5 μm. DiI-C18, 1,1'-dioctadecyl-3,3,3',3'-tetramethylindocarbocyanine perchlorate; DOPC, 1,2-dioleoyl-sn-glycero-3-phosphocholine; DPCC, 1,2-dipalmitoyl-sn-glycero-3-phosphocholine.

treated SH-SY5Y cells labeled with DiI-C_{18} show an increase in D from 2.51 ± 0.56 $\mu m^2/s$ to 4.34 ± 1.54 $\mu m^2/s$ (Fig. 1C, D). However, there was no visible aggregate formation in the cell membrane even 30 min posttreatment. In the case of GFP-GPI expressed in SH-SY5Y cells, heptanol treatment resulted in an increase in D from 0.83 ± 0.06 $\mu m^2/s$ to 1.72 ± 0.47 $\mu m^2/s$ (Fig. 1E, F). After incubating the sample for 15 min, we observed phase separation on the cell membrane in the form of GPI clusters. Altered lateral segregation in the form of domain stabilization could be due to the immiscibility of domain components caused by hyperfluidity of the membrane.

### Heptanol stabilizes phase separation in live PMs

Based on our results, we hypothesized that *heptanol-induced hyperfluidization stabilizes the phase separation in PMs resulting in the formation of micron-sized clusters of the phases, as they exist at the nanoscale.* To test this hypothesis, we studied the effect of heptanol on the lateral segregation of molecules with known localization preference. Since heptanol induces microscopic changes in the lateral organization of molecules, TIRF images are sufficient to determine the molecular rearrangements on the membrane.

Here, we probed the effect of heptanol on the organization of rhodamine-Cl8 (R-18), a lipophilic dye containing a single l8-membered hydrocarbon chain. It is excluded from the L_o environments and thus is regarded as a marker of the L_d phase (39). Owing to its lipophilic nature, this dye forms nonspecific clusters in untreated cell membranes (**Fig. 2**A). Upon heptanol treatment, we observed no additional cluster formation, and the cell membrane remained homogeneous, even 30 min after treatment (Fig. 2A).

CTxB has emerged as a commonly studied domain-binding protein (27, 54). It binds to GM1-ganglioside, a ubiquitous cell surface glycolipid residing in the L_o phase of the membrane. To test the effect of heptanol on the lateral segregation of CTxB, we treated CTxB-labeled SH-SY5Y cells with heptanol and imaged them 15 min posttreatment. In this case, we observed the formation of clusters on cell membranes (Fig. 2B). CTxB forms nonspecific clusters even in resting cell membranes. Thus, here we report the obvious increase in the number/size of clusters upon heptanol treatment. These experiments reveal the lateral segregation of endogenous GM1 molecules labeled by CTxB.

To further verify our hypothesis, we examined the effect of heptanol on the lateral segregation of two versions of the TMD of the linker for activation of T-cells (trLAT). The partitioning properties of wild-type (WT) and various mutants of trLAT were extensively characterized by Lorent *et al.* (17). It was shown that the WT-trLAT preferentially resides in the L_o phase of the cell membrane while the construct where all the TMD residues were mutated to leucine (allL-trLAT) showed dramatically decreased affinity to the L_o phase. Due to the existing knowledge regarding the partitioning of these constructs, we analyzed their
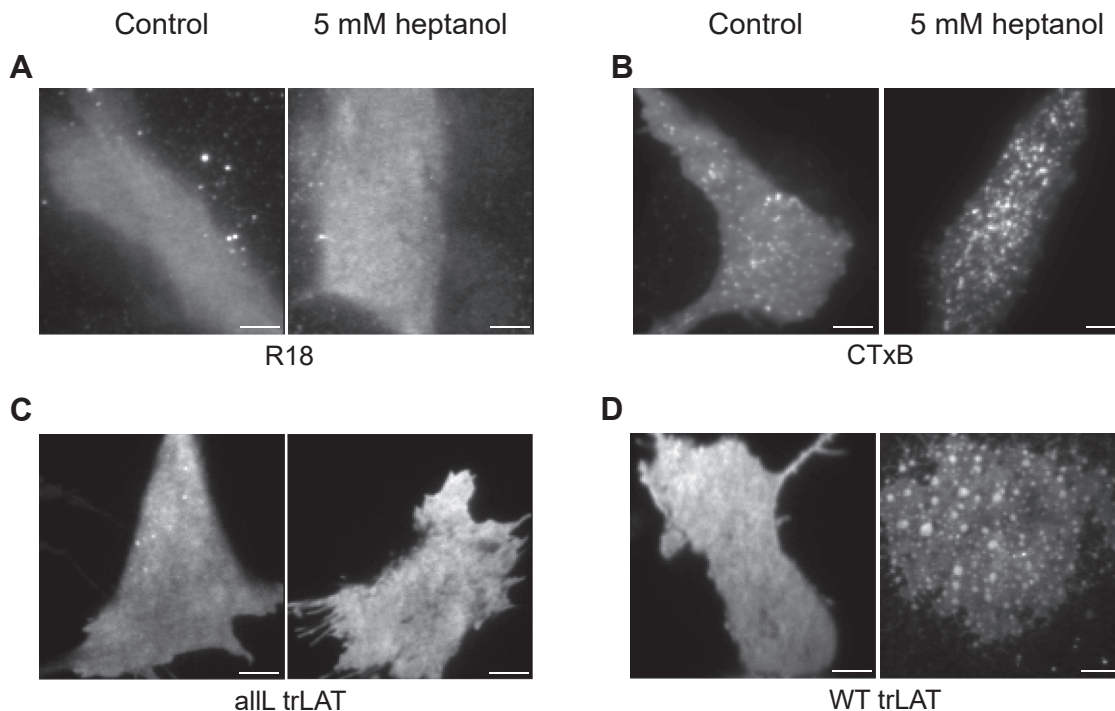
Fig. 2. Heptanol phase separates molecules based on their domain preference. Representative TIRF images of probe organization on SH-SY5Y cells before and after 5 mM heptanol treatment. A: Rhodamine 18 (R18). B: Cholera toxin B (CTxB). C: allL-trLAT. D: WT-trLAT. Experiments were repeated at least three times. The scale bars represent 5 μm. trLAT, transmembrane domain of linker for activation of T-cells.

organization upon heptanol treatment. We transfected these constructs in SH-SY5Y cells and recorded cell membrane images using total internal reflection fluorescence microscopy before and after treatment. In untreated cell membranes, WT-trLAT exhibits homogeneous expression, while allL-trLAT is extremely sensitive to the total protein amount transfected in the cell and often shows clusters at higher protein concentrations (Fig. 2C, D). The concentration of allL-trLAT plasmid was optimized to achieve a sufficient signal-to-noise ratio and minimal nonspecific clustering. Consistent with our hypothesis, we observed that in the case of WT-trLAT, heptanol induced formation of clusters in the cell membrane while allL-trLAT did not undergo any additional clustering in response to heptanol treatment (Fig. 2C, D).

Our results show that the lateral segregation of proteins/markers that preferentially reside in the L_o phase is affected in response to treatment with heptanol, and these molecules form microscopic clusters in the cell membrane. This is in accordance with our hypothesis that hyperfluidization of the PM induced by heptanol leads to stabilized phase separation in membranes. These experiments show that heptanol-mediated phase separation allows determining the phase preference of molecules that are transfected in cells or are labeled directly by an extrinsic label as in case of CTxB.

Domain preference of signaling-related proteins as determined by heptanol-induced phase separation

After validating that heptanol treatment can identify the phase preference of marker proteins in live cell membranes, we used this method to determine the phase preference of signaling-related proteins. We specifically focused on those proteins for which preexisting knowledge regarding their phase preference is available.

H-Ras and K-Ras are GTPases that function as molecular switches in the transduction of extracellular signals to the cytoplasm and nucleus. The membrane anchor in H-Ras consists of palmitoylated cysteine residues, thus directing it to the L_o phase in the membrane (55). In contrast, K-Ras consists of a polybasic domain of six contiguous lysines, which confers L_d preference to this protein (55). We transfected the SH-SY5Y cells with H-Ras and K-Ras constructs and treated the cells with heptanol. In untreated cells, H-Ras and K-Ras showed homogenous expression over the whole cell membrane. In heptanol-treated cells, as expected, H-Ras undergoes clustering upon heptanol treatment, while K-Ras does not (Fig. 3A, B).

Interleukin-2 (IL-2) signaling is directly regulated by the differential localization of IL-2Rβ–IL-2Rγ complexes in the soluble fraction of the membrane, i.e., L_d phase, while IL-2Rα is enriched in lipid microdomains, i.e., L_o phase of the membrane. Upon activation, three subunits of IL-2R heterotrimerize in the soluble

fraction of the membrane (56). Since phase preference of IL-2Rα is known, we subjected it to heptanol treatment and imaged changes in its lateral organization. IL-2Rα was homogenously expressed in untreated SH-SY5Y cells (Fig. 3C). As expected, heptanol treatment induced cluster formation also in this case (Fig. 3C), thus validating our hypothesis.

Further, we probed the localization of EGFR, a well-studied protein; however, its membrane organization is not fully known. EGFR has been shown to localize in cholesterol-dependent domains (13, 43, 57–59). However, previous work from our group showed that EGFR only partially depends on cholesterol-dependent
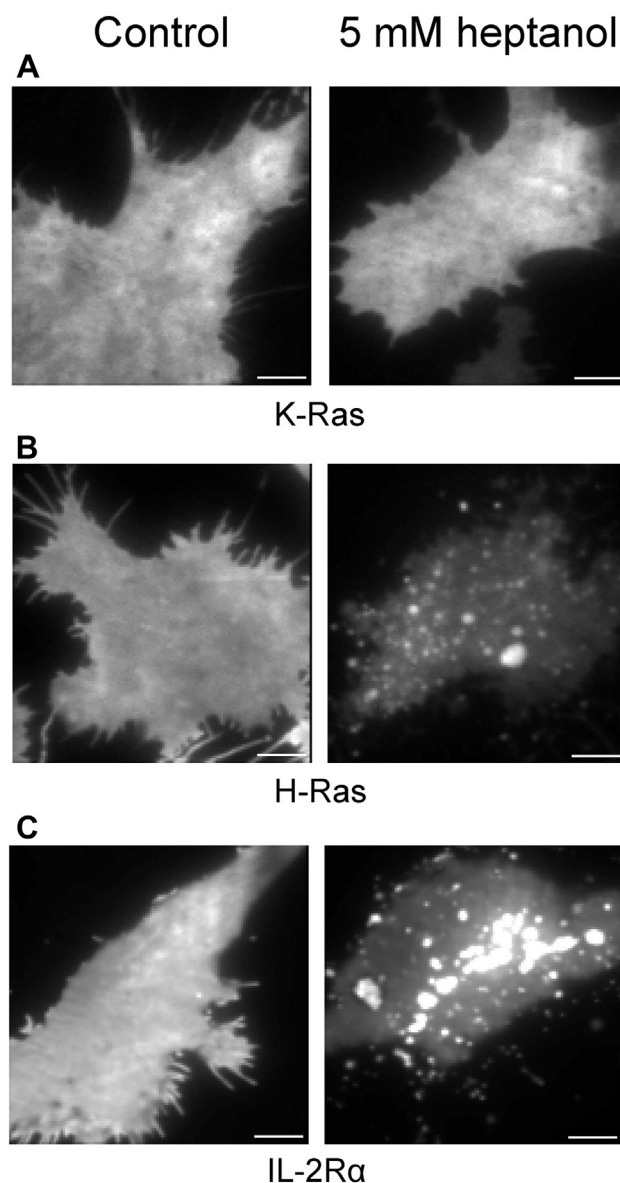
Fig. 3. Domain preference of signaling related proteins as determined by heptanol-induced phase separation. Representative TIRF images of protein organization on SH-SY5Y cells before and after 5 mM heptanol treatment. A: K-Ras. B: H-Ras. C: IL-2Rα. Experiments were repeated at least three times. The scale bars represent 5 μm.

ASBMB

domains ([13](#)), thus indicating the presence of EGFR molecules also resides in the cholesterol-independent fraction of the cell membrane. To gain more insights regarding the EGFR localization, we treated SH-SY5Y cells expressing EGFR with heptanol. Our results show that heptanol treatment leads to the formation of more clusters than those that were present before the treatment (**Fig. 4**A, B, supplemental Figs. S1 and S2A, B).

Since the concentration of heptanol is well above physiological concentrations used in anesthesia, we tested whether cells retain their integrity and remain viable after heptanol treatment. For that, we imaged cell morphology and visualized actin cytoskeleton organization marked by Lifeact-mRFPruby before and after heptanol treatment. Lifeact is a short 17 amino acid peptide that binds to actin ([44](#)). We found no significant differences in the morphology of cells and no microscopic differences in actin organization (supplemental Figs. S3 and S4). We also observed that the live cell fractions after trypan blue staining were similar for control and heptanol-treated cells at $92 \pm 10\%$ and $87 \pm 5\%$, respectively (n = 3). Furthermore, we performed Western blot analysis to probe for EGFR activation (phosphorylation) upon EGF stimulation in heptanol-treated cells. Cells responded to EGF stimulation and were able to signal even after heptanol treatment as indicated by the presence of phosphorylated EGFR. This suggests that the cells are viable (supplemental Fig. S5). To understand what proportion of cells respond to heptanol treatment, we performed imaging of larger fields of view, and we observed that a majority of the cells expressing L_o domain components show clustering in response to heptanol treatment (supplemental Fig. S6).

Comparison of cluster area fraction and cluster sizes for various probes

We compared the area fraction covered by clusters and cluster sizes on cell membranes expressing various probes—GPI, WT-trLAT, and EGFR—before and after heptanol treatment (supplemental Fig. S1). In resting cells, the samples exhibit almost homogeneous lateral segregation of molecules, and clusters cover $3 \pm 3\%$, $2 \pm 0.1\%$ and $2 \pm 2\%$ of the total cell membrane area for GPI, WT-trLAT, and EGFR, respectively. After heptanol treatment, the area fraction covered by clusters increased to $20 \pm 8\%$, $37 \pm 3\%$, and $10 \pm 2\%$, respectively ($P < 0.5$ in all cases; refer supplemental Fig. S1). The smaller increase for EGFR compared to GPI and WT-trLAT could be because of a population of EGFR that resides in the L_d phase ([13](#), [43](#), [58](#)). However, this requires further investigation.

All samples showed a similar range of 0.6–1 µm cluster size in both resting and treated cells ($P > 0.5$; refer supplemental Fig. S1). It is important to note that since the cluster area fraction is <5% in resting cells, which is significantly less than the cluster area fraction measured post heptanol treatment, these values

correspond to the size of some rarely occurring clusters on the membrane.

EGFR was also labeled with an antibody conjugated with Alexa 488 dye. The antibody labeling induced some clustering ($12 \pm 1\%$) of EGFR (Fig. 4C, supplemental Figs. S1 and S2C). The clustering increased upon heptanol addition ($24 \pm 5\%$; $P < 0.5$), indicating heptanol-induced phase separation (Fig. 4D, supplemental Figs. S1 and S2D). Therefore, MFIC can also be used with extrinsic fluorescent tags and does not require genetic labeling.

Heptanol-based assay to determine phase preference of membrane molecules is fast and reversible

Although microscopic clustering of molecules is typically observed 10–15 min after treatment, the immiscibility of phases starts immediately after addition of heptanol. This was revealed by our ITIR-FCS measurements consisting of 300,000 frames with an exposure time of 1 ms, i.e., dynamics readouts of 5 min. In these FCS videos ([60](#)), the first 50,000 frames were recorded on untreated cells, and then cells were treated with heptanol while recording the data. The heptanol-induced changes in membrane dynamics were then recorded for the subsequent 250,000 frames. We performed these experiments on WT-trLAT and allL-trLAT expressing SH-SY5Y cells and then utilized diffusion maps calculated from consecutive, nonoverlapping sections of 50,000 frames.

In the case of WT-trLAT, the first 50,000 frames show a homogeneous diffusion in the cell membrane. Upon heptanol treatment, there was an increase in D with time, indicating an increase in fluidity (supplemental Fig. S7A). Moreover, we observed that from 200,000 frames onwards, pixels appeared with high D, indicated by the separation of the high D pixels (*green* and *red*) from the cluster of pixels with low D (*blue*). However, TIRF images constructed from the projection of the last 50,000 frames did not show any noticeable microscopic clustering. Clustering of molecules was observed 10–15 min post heptanol treatment, only. This implies that smaller clusters, which are difficult to observe via imaging, are detected by the effect on molecular dynamics already early on.

Similar to WT-trLAT, allL-trLAT showed homogeneous diffusion in the first 50,000 frames (supplemental Fig. S7B), and heptanol treatment increased the overall D of the molecules. But unlike WT-trLAT, in this case, there was no noticeable phase separation as even after 250,000 frames diffusion remained homogenous, indicating the absence of phase separation on the cell membrane. Interestingly, despite being a nondomain probe, allL-trLAT diffuses slower than WT-trLAT. This is because the presence of many leucine residues in the transmembrane region of allL-trLAT make it relatively unstable in the membrane environment and induces self-assembly. This causes the
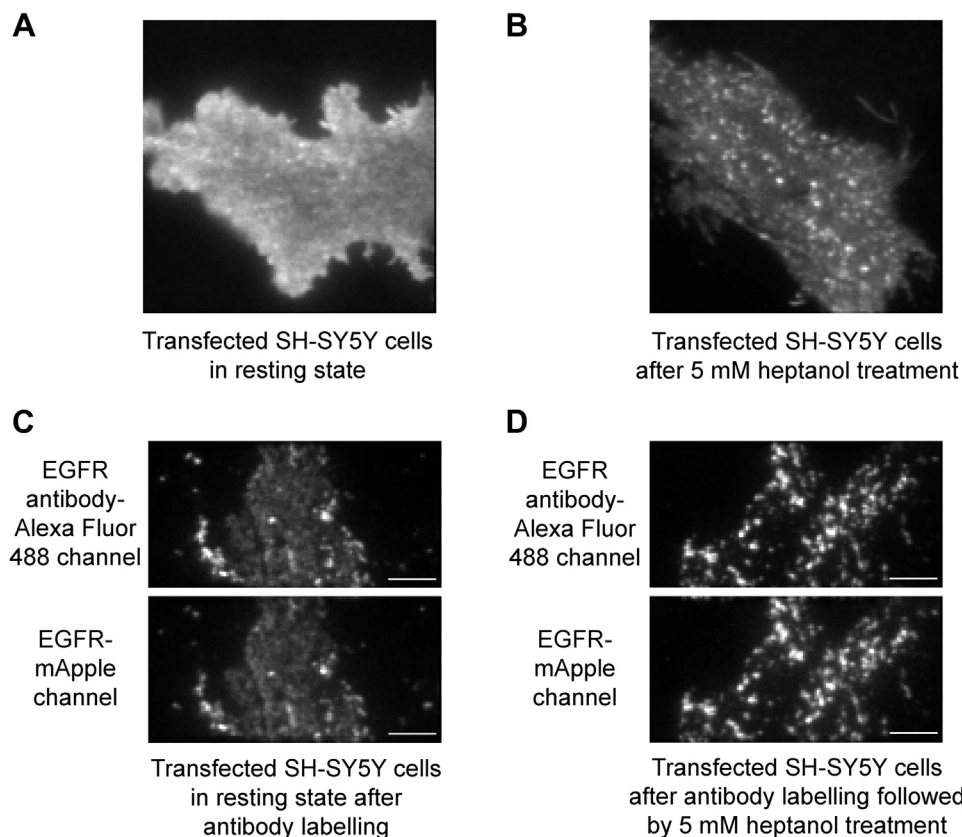
Fig. 4. Heptanol-induced phase separation of EGFR. Representative TIRF images of EGFR transfected SH-SY5Y cells under various conditions. A: EGFR-mEGFP in resting transfected cells. B: EGFR-mEGFP after 5 mM heptanol treatment. C: EGFR antibody-Alexa 488 and EGFR-mApple channels after labeling of resting cells with EGFR antibody. D: EGFR antibody-Alexa 488 and EGFR-mApple channels after labeling of the cells with EGFR antibody followed by 5 mM heptanol treatment. Experiments were repeated at least three times. The scale bars represent 5 μm. EGFR, epidermal growth receptor factor.

protein to cluster into small molecular aggregates which results in slower diffusion (61).

Next, we asked whether the L_o cluster regions, which are induced upon heptanol treatment, are accessible to molecules not preferentially located in these domains. For that, we performed TIRF imaging of cells expressing WT-trLAT-mEGFP and allL-trLAT-mApple. As observed in supplemental Fig. S8A, before heptanol treatment, both probes are homogeneously distributed on the membrane (supplemental Fig. S8A). Upon heptanol treatment, WT-trLAT-mEGFP starts clustering while allL-trLAT-mApple remains homogeneous, and no exclusion regions can be detected (supplemental Fig. S8B). This indicates that L_d components can access the L_o domains and traverse those regions. Moreover, it is important to note that there is no 100% partitioning of molecules as not all L_o molecules cluster and L_d molecules are present even in these clusters.

Next, we investigated the reversibility of heptanol treatment of cell membranes. A previous study has shown that the transfer rate of pyrenyl heptanol, a more lipophilic compound than heptanol, from membranes to water is around 200 milliseconds (62). Thus, it is expected that the reversal of heptanol-mediated fluidization should also initiate in a few milliseconds.

So, we wondered if heptanol-mediated membrane fluidization and reorganization is reversed upon washing of heptanol. To test this, we treated the cells with heptanol for 15 min, sufficient for cluster formation to occur. Then, we washed the heptanol solution from the cell membranes and incubated the cells for 24 h in complete growth medium at 37°C with 5% CO_2. We observed that 24 h after washing away the heptanol solution, the clusters had disappeared almost completely (supplemental Fig. S9), demonstrating the partially reversible nature of this assay. Despite the expected fast transfer of heptanol between membranes and water, the overall membrane reorganization is slower as we observe microscopic reversal of membrane reorganization only after much longer times. Also, it is to be noted that currently we do not know the full nature of the clusters and whether protein interactions are involved in addition to phase separation in their formation.

Furthermore, we asked if this result is obtainable in cell membranes other than SH-SY5Y. Hence, we transfected WT-trLAT and allL-trLAT in HeLa cells and examined their lateral organization before and after heptanol treatment. As observed in SH-SY5Y cell membranes, WT-trLAT undergoes clustering upon heptanol

treatment (supplemental Fig. S10A) while allL-trLAT does not show any microscopic changes in their organization in HeLa cell membranes (supplemental Fig. S10B).

DISCUSSION

Cell membrane organization results from the dynamic exchange between lipid–protein assemblies, monomeric proteins, oligomeric proteins, and lipid clusters. Maintenance of membrane dynamics is crucial for cellular functioning. Membrane residing molecules often prefer a specific phase environment; for instance, GPI-anchored proteins preferentially localize in cholesterol-dependent domains. Understanding the selective partitioning of molecules in membranes is one of the most challenging problems in membrane biology. Most routinely used methods to determine membrane localization of molecules, such as detergent-resistant membrane extraction, membrane extraction followed by mass spectrometry, and immunostaining, are time-consuming and are artifact-prone. Fluidizers present a promising alternative. Fluidizers such as benzyl alcohol, propofol, and heptanol have been shown to alter the membrane lipid dynamics by increasing the fluidity of the membrane and by reorganizing the membrane domains (50, 52, 63). The effects of fluidizers on membrane dynamics vary with their concentration and temperature. Here, we have developed and validated MFIC, a novel live-cell assay for determining the phase localization of proteins in cell membranes using heptanol. We demonstrate that heptanol induces membrane fluidization and stabilizes phase separation in cell membranes resulting in formation of microscopic clusters of L_o domains which are easy to detect by routine imaging methods. To test the ability of this assay in determining a molecule's phase preference, we carried out heptanol treatment on fluorescently labeled lipids and proteins for which phase preference is known (Figs. 2–4). Compared to the existing methods of ascertaining molecular phase preference, this method is fast as one obtains results within 15 min post heptanol treatment. Moreover, this method is less artifact-prone as it is carried out in live cell membranes. Heptanol-treated cells remain viable and continue signaling suggesting a limited influence on cell function (supplemental Figs. S3–S5). MFIC can be implemented on genetically fluorescence-labeled molecules as well as on endogenously expressed molecules labeled extrinsically, as demonstrated by experiments performed on CTxB and EGFR (Figs. 2 and 4).

The heptanol-induced membrane reorganization that we observe is consistent with previous computational and experimental studies in synthetic and purified membranes that show preferential partitioning of short-chain alcohols (<8 carbons) into the L_d phase and stabilization of phase separation in membranes (64, 65). Unlike our observations in live cell membranes, in vesicles, octanol had an opposite effect (66), suggesting membrane

vesicles might not retain all properties of live cell membranes, as has been shown in the case of membrane diffusion and organization (29, 67). Thus, approaches that allow the assessment of selective partitioning of molecules in a live cell membrane environment are well suited to address outstanding research questions in membrane biology and are invaluable for the field.

In conclusion, MFIC will aid in the quick and physiologically relevant identification of protein phase preference in cell membranes. Due to these attributes of MFIC, it is possible to conduct it at large-scale. It remains to be seen whether MFIC can be performed with different fluidizers to optimize assay time and signal-to noise ratio and whether it can be extended to a wider set of biological tissues, including other cell types, tissues, and organisms.

Author ORCIDs
Anjali Gupta https://orcid.org/0000-0002-9860-6312
Harikrushnan Balasubramanian https://orcid.org/0000-0003-4966-0221
Thorsten Wohland https://orcid.org/0000-0002-0148-4321

Abbreviations
CTxB, cholera toxin subunit B; DiI-C18, 1,1′-dioctadecyl-3,3,3′,3′-tetramethylindocarbocyanine perchlorate; DMEM, Dulbecco's Modified Eagle Medium; DOPC, 1,2-dioleoyl-sn-glycero-3-phosphocholine; DPPC, 1,2-dipalmitoyl-sn-glycero-3-phosphocholine; EGFR, epidermal growth factor receptor; EMCCD, electron multiplying charge-coupled device; FCS,

fluorescence correlation spectroscopy; GPI, glycosylphosphatidylinositol; mEGFP, monomeric enhanced green fluorescent protein; MFIC, membrane fluidizer-induced clustering; PM, plasma membrane; trLAT, transmembrane domain of linker for activation of T-cells.

REFERENCES

1. Lingwood, D., and Simons, K. (2010) Lipid rafts as a membrane-organizing principle. *Science.* **327**, 46–50
2. Lingwood, D., Kaiser, H. J., Leventa, I., and Simons, K. (2009) Lipid rafts as functional heterogeneity in cell membranes. *Biochem. Soc. Trans.* **37**, 955–960
3. Kusumi, A., Suzuki, K. G. N., Kasai, R. S., Ritchie, K., and Fujiwara, T. K. (2011) Hierarchical mesoscale domain organization of the plasma membrane. *Trends Biochem. Sci.* **36**, 604–615
4. Freeman, S. A., Vega, A., Riedl, M., Collins, R. F., Ostrowski, P. P., Woods, E. C., *et al.* (2018) Transmembrane pickets connect cyto- and pericellular skeletons forming barriers to receptor engagement. *Cell.* **172**, 305–317.e10
5. Brown, E. N., Purdon, P. L., and Van Dort, C. J. (2011) General anesthesia and altered states of arousal: a systems neuroscience analysis. *Annu. Rev. Neurosci.* **34**, 601–628
6. Chitilian, H. V., Eckenhoff, R. G., and Raines, D. E. (2013) Anesthetic drug development: novel drugs and new approaches. *Surg. Neurol. Int.* **4 (Suppl 1)**, S2–S10
7. Mitchell, D. C., Lawrence, J. T. R., and Litman, B. J. (1996) Primary alcohols modulate the activation of the G protein-coupled receptor rhodopsin by a lipid-mediated mechanism. *J. Biol. Chem.* **271**, 19033–19036
8. Hulse, D., Kusel, J. R., O'Donnell, N. G., and Wilkinson, P. C. (1994) Effects of anaesthetics on membrane mobility and locomotor responses of human neutrophils. *FEMS Immunol. Med. Microbiol.* **8**, 241–248
9. Gupta, A., Marzinek, J. K., Jefferies, D., Bond, P. J., Harryson, P., and Wohland, T. (2019) The disordered plant dehydrin Lti30 protects the membrane during water-related stress by cross-linking lipids. *J. Biol. Chem.* **294**, 6468–6482
10. Seeman, P. (1972) The membrane actions of anesthetics and tranquilizers. *Pharmacol. Rev.* **24**, 583–655
11. Ingólfsson, H. I., and Andersen, O. S. (2011) Alcohol's effects on lipid bilayer properties. *Biophys. J.* **101**, 847–855
12. Pralle, A. (2020) Modulation and dynamics of cell membrane heterogeneities. *Chem. Phys. Lipids.* **233**, 105006
13. Bag, N., Huang, S., and Wohland, T. (2015) Plasma membrane organization of epidermal growth factor receptor in resting and ligand-bound states. *Biophys. J.* **109**, 1925–1936
14. Cheng, P. C., Dykstra, M. L., Mitchell, R. N., and Pierce, S. K. (1999) A role for lipid rafts in B cell antigen receptor signaling and antigen targeting. *J. Exp. Med.* **190**, 1549–1560
15. Stone, M. B., Shelby, S. A., Núñez, M. F., Wisser, K., and Veatch, S. L. (2017) Protein sorting by lipid phase-like domains supports emergent signaling function in B lymphocyte plasma membranes. *Elife.* **6**, e19891
16. Escribá, P. V., Wedegaertner, P. B., Goñi, F. M., and Vögler, O. (2007) Lipid-protein interactions in GPCR-associated signaling. *Biochim. Biophys. Acta Biomembr.* **1768**, 836–852
17. Lorent, J. H., Diaz-Rohrer, B., Lin, X., Spring, K., Gorfe, A. A., Leventa, K. R., *et al.* (2017) Structural determinants and functional consequences of protein affinity for membrane rafts. *Nat. Commun.* **8**, 1–9
18. Kwik, J., Boyle, S., Fooksman, D., Margolis, L., Sheetz, M. P., and Edidin, M. (2003) Membrane cholesterol, lateral mobility, and the phosphatidylinositol 4,5-bisphosphate-dependent organization of cell actin. *Proc. Natl. Acad. Sci. U. S. A.* **100**, 13964–13969
19. Kenworthy, A. K. (2008) Have we become overly reliant on lipid rafts? Talking point on the involvement of lipid rafts in T-cell activation. *EMBO Rep.* **9**, 531–535
20. Maula, T., Al Sazzad, M. A., and Slotte, J. P. (2015) Influence of hydroxylation, chain length, and chain unsaturation on bilayer properties of ceramides. *Biophys. J.* **109**, 1639–1651
21. Benda, A., Beneš, M., Mareček, V., Lhotsk, A., Hermens, W. T., and Hof, M. (2003) How to determine diffusion coefficients in planar phospholipid systems by confocal fluorescence correlation spectroscopy. *Langmuir.* **19**, 4120–4126
22. Honigmann, A., Mueller, V., Ta, H., Schoenle, A., Sezgin, E., Hell, S. W., *et al.* (2014) Scanning STED-FcS reveals spatiotemporal heterogeneity of lipid interaction in the plasma membrane of living cells. *Nat. Commun.* **5**, 5412
23. García-Sáez, A. J., Chiantia, S., and Schwille, P. (2007) Effect of line tension on the lateral organization of lipid membranes. *J. Biol. Chem.* **282**, 33537–33544
24. Chiantia, S., Kahya, N., Ries, J., and Schwille, P. (2006) Effects of ceramide on liquid-ordered domains investigated by simultaneous AFM and FCS. *Biophys. J.* **90**, 4500–4508
25. Maté, S., Busto, J. V., García-Arribas, A. B., Sot, J., Vazquez, R., Herlax, V., *et al.* (2014) N-Nervonoylsphingomyelin (C24:1) prevents lateral heterogeneity in cholesterol-containing membranes. *Biophys. J.* **106**, 2606–2616
26. Benda, A., Faguľová, V., Deyneka, A., Enderlein, J., and Hof, M. (2006) Fluorescence lifetime correlation spectroscopy combined with lifetime tuning: new perspectives in supported phospholipid bilayer research. *Langmuir.* **22**, 9580–9585
27. Bacia, K., Scherfeld, D., Kahya, N., and Schwille, P. (2004) Fluorescence correlation spectroscopy relates rafts in model and native membranes. *Biophys. J.* **87**, 1034–1043
28. Honigmann, A., Sadeghi, S., Keller, J., Hell, S. W., Eggeling, C., and Vink, R. (2014) A lipid bound actin meshwork organizes liquid phase separation in model membranes. *Elife.* **3**, e01671
29. Sezgin, E., Leventa, I., Grzybek, M., Schwarzmann, G., Mueller, V., Honigmann, A., *et al.* (2012) Partitioning, diffusion, and ligand binding of raft lipid analogs in model and cellular plasma membranes. *Biochim. Biophys. Acta.* **1818**, 1777–1784
30. Su, X., Ditlev, J. A., Hui, E., Xing, W., Banjade, S., Okrut, J., *et al.* (2016) Phase separation of signaling molecules promotes T cell receptor signal transduction. *Science.* **352**, 595–599
31. London, E., and Brown, D. A. (2000) Insolubility of lipids in Triton X-100: physical origin and relationship to sphingolipid/cholesterol membrane domains (rafts). *Biochim. Biophys. Acta.* **1508**, 182–195
32. Schnell, U., Dijk, F., Sjollema, K. A., and Giepmans, B. N. G. (2012) Immunolabeling artifacts and the need for live-cell imaging. *Nat. Methods.* **9**, 152–158
33. Harkewicz, R., and Dennis, E. A. (2011) Applications of mass spectrometry to lipids and membranes. *Annu. Rev. Biochem.* **80**, 301–325
34. Gupta, A., Korte, T., Herrmann, A., and Wohland, T. (2020) Plasma membrane asymmetry of lipid organization: fluorescence lifetime microscopy and correlation spectroscopy analysis. *J. Lipid Res.* **61**, 252–266
35. Gupta, A., Muralidharan, S., Torta, F., Wenk, M. R., and Wohland, T. (2020) Long acyl chain ceramides govern cholesterol and cytoskeleton dependence of membrane outer leaflet dynamics. *Biochim. Biophys. Acta Biomembr.* **1862**, 183153
36. Huang, S., Lim, S. Y., Gupta, A., Bag, N., and Wohland, T. (2017) Plasma membrane organization and dynamics is probe and cell line dependent. *Biochim. Biophys. Acta Biomembr.* **1859**, 1483–1492
37. Dinic, J. (2011) Plasma Membrane Order; the Role of Cholesterol and Links to Actin Filaments. Thesis, Stockholm University, Stockholm, Sweden
38. Gidwani, A., Holowka, D., and Baird, B. (2001) Fluorescence anisotropy measurements of lipid order in plasma membranes and lipid rafts from RBL-2H3 mast cells. *Biochemistry.* **40**, 12422–12429
39. Klymchenko, A. S., and Kreder, R. (2014) Fluorescent probes for lipid rafts: from model membranes to living cells. *Chem. Biol.* **21**, 97–113
40. Gupta, A., Phang, I. Y., and Wohland, T. (2020) To hop or not to hop: exceptions in the FCS Diffusion law. *Biophys. J.* **118**, 2434–2447
41. Šachl, R., Bergstrand, J., Widengren, J., and Hof, M. (2016) Fluorescence correlation spectroscopy diffusion laws in the presence of moving nanodomains. *J. Phys. D Appl. Phys.* **49**, 114002

ASBMB

42. Sevcsik, E., Brameshuber, M., Fölser, M., Weghuber, J., Honigmann, A., and Schütz, G. J. (2015) GPI-anchored proteins do not reside in ordered domains in the live cell plasma membrane. *Nat. Commun.* **6**, 1–10

43. Sankaran, J., Balasubramanian, H., Tang, W. H., Ng, X. W., Röllin, A., and Wohland, T. (2021) Simultaneous spatiotemporal super-resolution and multi-parametric fluorescence microscopy. *Nat. Commun.* **12**, 1748

44. Riedl, J., Crevenna, A. H., Kessenbrock, K., Yu, J. H., Neukirchen, D., Bista, M., *et al.* (2008) Lifeact: a versatile marker to visualize F-actin. *Nat. Methods.* **5**, 605–607

45. Diaz-Rohrer, B. B., Leventall, K. R., Simons, K., and Leventall, I. (2014) Membrane raft association is a determinant of plasma membrane localization. *Proc. Natl. Acad. Sci. U. S. A.* **111**, 8500–8505

46. Sankaran, J., Balasubramanian, H., Tang, W. H., Ng, X. W., Röllin, A., and Wohland, T. (2021) Preparation of live cell samples for fluorescence spectroscopy and computational super-resolution imaging. *Protoc. Exch.* https://doi.org/10.21203/rs.3.pex-1357/v1

47. Sankaran, J., Balasubramanian, H., Tang, W. H., Ng, X. W., Röllin, A., and Wohland, T. (2021) Simultaneous spatiotemporal computational super-resolution and multi-parametric fluorescence microscopy. *Protoc. Exch.* https://doi.org/10.21203/rs.3.pex-1358/v1

48. Kapur, J. N., Sahoo, P. K., and Wong, A. K. C. (1985) A new method for gray-level picture thresholding using the entropy of the histogram. *Comput. Vis. Graph. Image Process.* **29**, 273–285

49. Lange, Y., Ye, J., Duban, M. E., and Steck, T. L. (2009) Activation of membrane cholesterol by 63 amphipaths. *Biochemistry.* **48**, 8505–8515

50. Nagy, E., Balogi, Z., Gombos, I., Åkerfelt, M., Björkbom, A., Balogh, G., *et al.* (2007) Hyperfluidization-coupled membrane microdomain reorganization is linked to activation of the heat shock response in a murine melanoma cell line. *Proc. Natl. Acad. Sci. U. S. A.* **104**, 7945–7950

51. Muddana, H. S., Chiang, H. H., and Butler, P. J. (2012) Tuning membrane phase separation using nonlipid amphiphiles. *Biophys. J.* **102**, 489–497

52. Jin, W., Zucker, M., and Pralle, A. (2021) Membrane nanodomains homeostasis during propofol anesthesia as function of dosage and temperature. *Biochim. Biophys. Acta Biomembr.* **1863**, 183511

53. Veatch, S. L., and Keller, S. L. (2003) Separation of liquid phases in giant vesicles of ternary mixtures of phospholipids and cholesterol. *Biophys. J.* **85**, 3074–3083

54. Day, C. A., and Kenworthy, A. K. (2015) Functions of cholera toxin B-subunit as a raft cross-linker. *Essays Biochem.* **57**, 135–145

55. Prior, I. A., Harding, A., Yan, J., Sluimer, J, Parton, R. G., and Hancock, J. F. (2001) GTP-dependent segregation of H-ras from lipid rafts is required for biological activity. *Nat. Cell Biol.* **3**, 368–375

56. Marmor, M. D., and Julius, M. (2001) Role for lipid rafts in regulating interleukin-2 receptor signaling. *Blood.* **98**, 1489–1497

57. Irwin, M. E., Mueller, K. L., Bohin, N., Ge, Y., and Boerner, J. L. (2011) Lipid raft localization of EGFR alters the response of cancer cells to the EGFR tyrosine kinase inhibitor gefitinib. *J. Cell. Physiol.* **226**, 2316–2328

58. Pike, L. J., and Casey, L. (2002) Cholesterol levels modulate EGF receptor-mediated signaling by altering receptor function and trafficking. *Biochemistry.* **41**, 10315–10322

59. Pike, L. J. (2005) Growth factor receptors, lipid rafts and caveolae: an evolving story. *Biochim. Biophys. Acta.* **1746**, 260–273

60. Bag, N., Ali, A., Chauhan, V. S., Wohland, T., and Mishra, A. (2013) Membrane destabilization by monomeric hIAPP observed by imaging fluorescence correlation spectroscopy. *Chem. Commun.* **49**, 9155–9157

61. Gurezka, R., Laage, R., Brosig, B., and Langosch, D. (1999) A heptad motif of leucine residues found in membrane proteins can drive self-assembly of artificial transmembrane segments. *J. Biol. Chem.* **274**, 9265–9270

62. Pownall, H. J., Hickson, D. L., and Smith, L. C. (1983) Transport of biological lipophiles: effect of lipophile structure. *J. Am. Chem. Soc.* **105**, 2440–2445

63. Balogh, G., Horváth, I., Nagy, E., Hoyk, Z., Benkő, S., Bensaude, O., *et al.* (2005) The hyperfluidization of mammalian cell membranes acts as a signal to initiate the heat shock protein response. *FEBS J.* **272**, 6077–6086

64. Centi, A., Dutta, A., Parekh, S. H., and Bereau, T. (2020) Inserting small molecules across membrane mixtures: insight from the potential of mean force. *Biophys. J.* **118**, 1321–1332

65. Cornell, C. E., McCarthy, N. L. C., Leventall, K. R., and Leventall, I. (2017) n-Alcohol length governs shift in Lo-Ld mixing temperatures in synthetic and cell-derived membranes. *Biophys. J.* **113**, 1200–1211

66. Gray, E., Karslake, J., and Machta, B. B. (2013) Liquid general anesthetics lower critical temperatures in plasma membrane vesicles. *Biophys. J.* **105**, 2751–2759

67. Schneider, F., Waithe, D., Clausen, M. P., Galiani, S., Koller, T., Ozhan, G., and Eggeling, C. (2017) Diffusion of lipids and GPI-anchored proteins in actin-free plasma membrane vesicles measured by STED-FCS. *Mol. Biol. Cell.* **28**, 1507–1518